

LETTER TO THE EDITOR

No country for old stars

Spectroscopic confirmation of the first intermediate-age RR Lyrae in the open cluster Trumpler 5

V. D’Orazi^{1,2,*,**}, C. Mateu^{3,*,**}, G. Iorio⁴, A. Bobrick^{5,6}, Z. Prudil⁷, R. Salinas⁸, A. Bragaglia⁹, L. Mashonkina¹⁰, R. G. Gratton¹¹, I. Ilyn¹², N. Alvarez Baena^{1,2}, V. F. Braga², A. Nunnari^{1,2}, V. M. Kalari¹³, F. Cusano⁹, and S. Tosi²

¹ Department of Physics, University of Rome Tor Vergata, via della Ricerca Scientifica 1, I-00133 Rome, Italy

² INAF – Osservatorio Astronomico di Roma, Via Frascati 33, Monte Porzio Catone I-00078, Italy

³ Departamento de Astronomía, Instituto de Física, Universidad de la República, Iguá 4225, CP 11400 Montevideo, Uruguay

⁴ Institut de Ciències del Cosmos (ICCUB), Universitat de Barcelona, c. Martí i Franquès 1, 08028 Barcelona, Spain

⁵ School of Physics and Astronomy, Monash University, Clayton, VIC 3800, Australia

⁶ Australian Research Council Centre of Excellence for Gravitational Wave Discovery, Clayton, VIC 3800, Australia

⁷ European Southern Observatory, Karl-Schwarzschild-Strasse 2, D-85748 Garching bei München, Germany

⁸ Nicolaus Copernicus Astronomical Center, Polish Academy of Sciences, Bartycka 18, 00-716 Warszawa, Poland

⁹ INAF – Osservatorio di Astrofisica e Scienza dello Spazio di Bologna, via P. Gobetti 93/3, I-40129 Bologna, Italy

¹⁰ Institute of Astronomy, Russian Academy of Sciences, 119017 Moscow, Russia

¹¹ INAF – Osservatorio Astronomico di Padova, vicolo dell’Osservatorio 5, I-35122 Padova, Italy

¹² Leibniz-Institut für Astrophysik Potsdam, An der Sternwarte 16, D-14482 Potsdam, Germany

¹³ Gemini Observatory/NSF’s NOIRLab, Casilla 603, La Serena, Chile

Received 6 April 2026 / Accepted 10 April 2026

ABSTRACT

Context. RR Lyrae (RRL) stars are widely considered tracers of ancient (>10 Gyr) metal-poor stellar populations. However, recent kinematic and photometric studies suggest the existence of a metal-rich RRL subpopulation associated with the thin disk and intermediate ages (~2–5 Gyr), therefore challenging canonical evolutionary models.

Aims. We aim to provide the first spectroscopic confirmation of a member of this elusive population. Specifically, we target a metal-rich RRL candidate recently identified photometrically as a member of the intermediate-age open cluster Trumpler 5 (~2.5 Gyr).

Methods. We obtained high-resolution spectroscopy using PEPsi at the LBT and GHOST at Gemini South telescope. We measured radial velocities (RVs) from multiple epochs to constrain cluster membership and derived detailed chemical abundances (Mg, Ca, Sc, Ti, Mn, Fe, Cu, Zn, Y, and Ba) to compare the RRL’s composition with that of red clump stars in the cluster.

Results. The RRL’s systemic velocity ($V_{\gamma} = 50.57^{+0.78}_{-0.36}$ km s⁻¹) is in excellent agreement with the cluster mean ($V = 50.76 \pm 0.49$ km s⁻¹). Combining RVs, proper motions, and parallax, the probability of the star being a background interloper is negligible (~0.002%, better than 4σ). We derived a metallicity of $[\text{Fe}/\text{H}] = -0.40 \pm 0.05$, which matches the cluster value. While most abundance ratios (Mg, Ti, Mn, Cu, and Zn) align with cluster members, the RRL exhibits significant depletion in Ca, Sc, Y, and Ba. Notably, $[\text{Sc}/\text{Fe}]$ is underabundant by ~0.6 dex relative to the cluster stars, following trends seen in field metal-rich RRLs.

Conclusions. We provide strong constraints on the membership status between an RRL variable and an intermediate-age open cluster. Cluster membership enables accurate measurement of RRL age and chemical anomalies relative to its host, particularly in Sc and neutron-capture elements. These anomalies further reinforce a nonstandard formation channel for this RRL, possibly indicating binary interactions and mass transfer.

Key words. stars: abundances – stars: variables: RR Lyrae – Galaxy: abundances – Galaxy: disk – open clusters and associations: individual: Trumpler 5

1. Introduction

RR Lyrae stars (RRLs) are low-mass core–helium-burning pulsators located on the horizontal branch of the Hertzsprung–Russell diagram (Preston 1964). Occupying the classical instability strip, they exhibit radial pulsations with characteristic

periods on the order a few tenths of a day (typically < 1 day; e.g., Catelan & Smith 2015) and provide important tests of stellar evolution and pulsation theory. In addition, RRLs are well-established standard candles. Their utility as distance indicators is underpinned by tight period–luminosity relations (see, e.g., Narloch et al. 2024). This property makes them essential for accurate distance determinations in the Milky Way and nearby galaxies as well as for tracing the formation and evolutionary history of the Galactic components (e.g., Neeley et al. 2019;

* Corresponding authors: vdorazi@roma2.infn.it; cmateu@fcien.edu.uy

** The first two authors contributed equally.

Bono et al. 2026). Canonical single-star evolutionary models suggest that RRLs are produced only in stellar systems that are both very old (ages $\gtrsim 9$ –10 Gyr) and sufficiently metal poor ($[\text{Fe}/\text{H}] \lesssim -0.5$). Under these conditions, the horizontal branch extends across the instability strip, allowing stars to enter the pulsation regime characteristic of RR Lyrae variables (e.g., Catelan & Smith 2015). The high incidence of RRLs in predominantly ancient environments – such as Galactic globular clusters, ultra-faint dwarf galaxies, and stellar halos – has reinforced the view that they trace exclusively old, metal-poor stellar populations. Beginning with Layden (1995) and further supported by Zinn et al. (2020), Prudil et al. (2020), and Iorio & Belokurov (2021), a substantial subset of metal-rich RRLs ($[\text{Fe}/\text{H}] \gtrsim -0.5$, extending to near-solar metallicities) has been identified. These stars exhibit kinematics consistent with a relatively young thin-disk component characterized by markedly colder and more rapidly rotating Galactic orbits than the >10 Gyr disk populations expected for canonical RRLs. Additional support comes from recent analyses of RRL kinematics in the warped outer disk (Cabrera-Gadea et al. 2025) and from comparisons between the kinematics of RR Lyrae and Mira variables of different ages, with the latter inferred from the Mira period–age relation (Zhāng et al. 2025). Furthermore, Cuevas-Otahola et al. (2025) identified 23 probable RR Lyrae members in ten intermediate-age (1–8 Gyr) clusters in the Large and Small Magellanic Clouds. However, the authors emphasize that spectroscopic confirmation is still required to secure their cluster membership.

Despite this converging evidence, current claims for intermediate-age RRLs remain based on indirect age diagnostics and population-statistical arguments rather than direct age determinations. Very recently, Mateu et al. (2025) (hereafter M25) reported the first detection of an RRL (Gaia DR3 3326852328563919744) associated with the intermediate-age (2–4 Gyr) open cluster (OC) Trumpler 5, found by cross-matching a large all-sky RRL compilation with kinematically selected members of over 3000 Gaia-based OCs. The multicolor light curves, parallax, proper motions, position within the cluster tidal radius, and location in the Gaia color–magnitude diagram are all consistent with cluster membership, with only a $\sim 0.05\%$ (or 3.5σ) probability of being a field interloper (see M25 for details). Nonetheless, the lack of spectroscopic constraints on its kinematics and chemical composition has so far prevented a fully secure association. In this paper, we present high-resolution spectroscopic observations of Mateu’s star and derive its radial velocity (RV) and detailed chemical abundances, conclusively confirming its membership in Trumpler 5.

2. Observations and analysis

The target RRL star was observed with the high-resolution PEPSI spectrograph (Strassmeier et al. 2015) on the Large Binocular Telescope (Mount Graham, Arizona) between October 2025 and February 2026 as part of a DDT program. The PEPSI observations used simultaneous spectral setups CD1+CD5 or CD2+CD4 (see Table A.1), yielding $R \approx 50\,000$; all spectra were used to measure RVs. However, CD1 and CD2 suffered from very low S/N, and the remaining CD4 or CD5 setups contain a limited number of usable lines because the RRL spectral energy distribution peaks toward blue wavelengths (~ 400 nm). To obtain chemical abundances, we therefore relied on additional observations with the new high-resolution GHOST spectrograph (Kalari et al. 2024) at Gemini South (Cerro Pachón, Chile). GHOST delivers $R \approx 45\,000$ (2×2 binning) and continuous coverage from 347–1061 nm with its blue

and red arms (see Table A.1). Exposures were limited to 1200 s; for parameter and abundance determination, we used only the spectrum obtained at $\phi \approx 0.3$ – the optimal phase for RRL abundance analysis (e.g., For et al. 2011) – which also has the highest S/N (highlighted in yellow in Table A.1). The determination of the RVs for each spectrum was performed using the cross-correlation algorithm in the 2023 version of iSpec (Blanco-Cuaresma et al. 2014).

Stellar parameters and elemental abundances were determined using PySME (Wehrhahn et al. 2023), a Python implementation of Spectroscopy Made Easy (Piskunov & Valenti 2017). This software allows for real-time computation of Non Local Thermodynamical Equilibrium (NLTE) synthetic spectra and employs a least-squares minimization procedure using the dog-box algorithm as implemented in *scipy* (Virtanen et al. 2020). The code provides error estimates for each parameter and abundance by calculating random and systematic uncertainties. The internal random error, which is dependent on the S/N of the spectra, can be readily determined from the least-squares fit in PySME using the covariance matrix. Systematic uncertainties were computed following the methodology outlined in Piskunov & Valenti (2017), but they are not relevant for this study, as our primary objective is to perform a differential analysis of the composition of our RRL relative to red clump (RC) stars in Trumpler 5. For our analysis, we employed model atmospheres from the MARCS grid (Gustafsson et al. 2008) and NLTE departure coefficients from Amarsi et al. (2020) for all elements except Ti and Cu (which were sourced from Mallinson et al. 2024 and Caliskan et al. 2025, respectively) and Sc. The departures from LTE for Sc were specifically calculated for this study by following the approach described in Mashonkina & Romanovskaya (2022). Abundances for Zn and Y are the only ones we report in LTE since departure coefficient grids are not available within the PySME framework.

We optimized the effective temperature (T_{eff}), surface gravity ($\log g$), microturbulence (V_{mic}), and macroturbulence (V_{mac}), along with the abundances of iron and titanium, using a comprehensive line list that includes Fe I, Fe II, Ti I, and Ti II lines (see Table B.1 for details). An example of our spectral synthesis, for a restricted range in wavelengths, is shown in Figure B.1. Subsequently, we adopted the derived stellar parameters and metallicity to infer the elemental abundances of Mg, S, Ca, Sc, Ti, Mn, Cu, Zn, Y, and Ba. To minimize the impact of systematic uncertainties in comparing abundances of our target RRL and the OC members, we retrieved two RC stars from the ESO archive, initially published in Donati et al. (2015). These spectra were obtained with UVES (D’Odorico et al. 2000) at the Very Large Telescope (VLT), featuring a nominal resolution of $R \approx 40\,000$ (slit width of 1.2 arcsec) and a spectral coverage of $\lambda\lambda$ 328–456 nm (CD#2) and 472–683 nm (CD#3). We analyzed these two stars using exactly the same methodology as for the RRL (i.e., identical line lists, model atmospheres, and radiative transfer code), thereby reducing systematic effects. The only exception is sulfur. The high-excitation triplet at 6743–6757 Å is too weak to be detected in the RC spectra, preventing an estimate of their S abundance.

3. Results and discussion

Radial velocities – The star’s systemic line-of-sight velocity (V_{γ}) was obtained by fitting the RV template from Prudil et al. (2024) to the phase-folded observations. The amplitude of the RV curve (AmpRV) and an additional velocity dispersion term (σ_x) were included as free parameters. Full details about

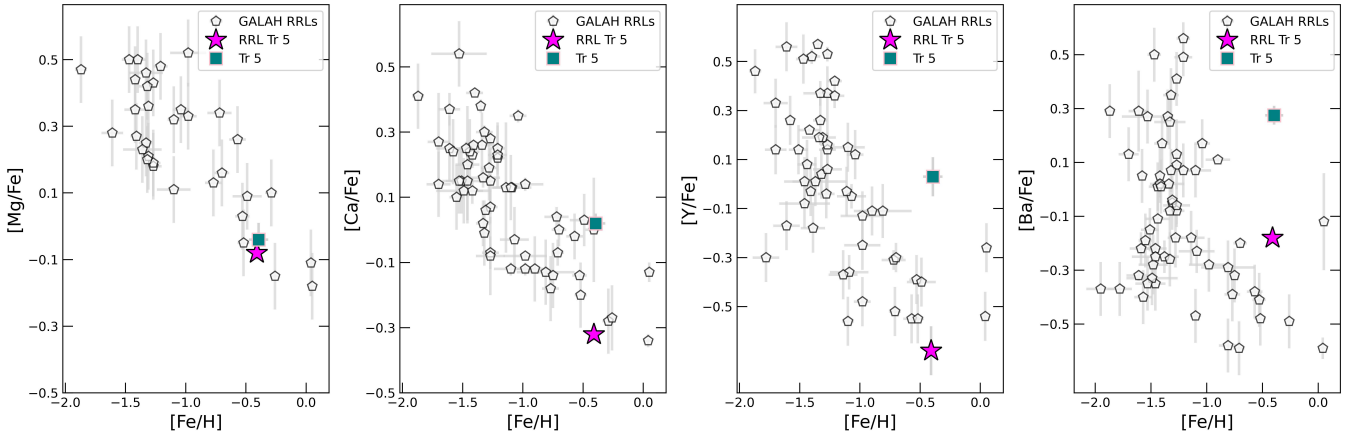


Fig. 1. $[X/Fe]$ for Mg, Ca, Y, and Ba as a function of $[Fe/H]$ for the RRL, the average of two RC stars in Trumpler 5, and for RRLs in the GALAH sample by D’Orazi et al. (2024).

the inference model can be found in Appendix E, including the phase-folded RV curve and residuals with respect to the best-fitting model. The best-fitting values found were $V_\gamma = 50.57^{+0.78}_{-0.36}$ km s⁻¹, $\text{AmpRV} = 54.6^{+3.1}_{-3.2}$ km s⁻¹, and $\sigma_x = 1.82^{+0.45}_{-0.35}$ km s⁻¹, which correspond to the maximum a posteriori (MAP) and uncertainties to 14th and 86th percentiles, respectively.

The systemic RV found for the Trumpler 5 RRL is in excellent agreement with the cluster mean reported by Özdemiř et al. (2025): 50.76 km s⁻¹, with a velocity dispersion of $\sigma_v = 0.49$ km s⁻¹. We can now use this result to compute an updated probability that a background RRL would be misidentified as a cluster member. The authors of M25 used RRLs within 25° of the cluster to model their distribution in parallax and proper motion and obtained a probability of 0.0049% that a random background star would have the same parallax and proper motion as the Trumpler 5 RRL. We included an RV factor, estimated from the background distribution from the selection of plausible RRL stars ($M_{\text{bol}} \in [0.45, 0.7]$ and $T_{\text{eff}} \in [6200, 7800]$ K) from the Gaia Universe Model and Gaia Object Generator simulations, and we modeled it with a Gaussian decomposition. This yielded a probability of $p = 0.0004\%$ that a random background RRL will have the same parallax, proper motion, and RV as ours (to within three times its uncertainties and the cluster’s velocity dispersion). Finally, considering there is one possible member out of a total of four RRLs within the cluster’s tidal radius, we obtained a binomial probability of 0.0017% for the star to be a random background interloper.

Elemental abundances – The stellar parameters and elemental abundances for our RRL, along with RC stars in Trumpler 5, are detailed in Table C.1. For the two RC stars, our retrieved stellar parameters and $[Fe/H]$ align closely with those of Donati et al. (2015), reinforcing the notion that significant systematic errors do not adversely affect our results. With the exception of manganese and barium – the former exhibits a deficit of approximately ~ -0.2 dex, while the latter shows an enhancement of about 0.25 dex – all other species display solar-scaled $[X/Fe]$ ratios, consistent with expectations for Population I stars. The enhancement of Ba in intermediate-age and young open clusters has been a persistent issue in the field, as discussed in D’Orazi et al. (2022, and references therein). We note, in passing, that the supersolar $[Ba/Fe]$ values supports our adopted age

of $\tau = 2.5$ Gyr rather than the older value of around 4 Gyr (see the extensive discussion in M25).

For the RRL star, we derived a metallicity of $[Fe/H] = -0.40 \pm 0.05$, in excellent agreement with the cluster value. When comparing abundance ratios, we found very good agreement in Mg, Ti, Mn, Cu, and Zn between the RRL and the OC stars (see Figure C.1). In contrast, Ca, Sc, Y, and Ba show significant discrepancies: The RRL exhibits notably subsolar $[X/Fe]$ ratios for these elements. Such differences in Ca, Y, and Ba between metal-rich RRLs and field giants and dwarfs have already been reported in the literature, including the recent GALAH DR3 sample of RRLs analyzed by D’Orazi et al. (2024). However, that work (as all the previous ones) compared field RRLs with field nonvariable stars, mixing populations of different ages, metallicities, and other abundances. Our study is the first to compare the chemical peculiarities of a metal-rich RRL directly with stars from the same cluster, thereby using well-constrained parent abundances and removing the mixed-population-related systematics. Figure 1 shows the comparison of $[X/Fe]$ for Mg, Ca, Y, and Ba of the target with RRLs in GALAH DR3. Mateu’s star lies in a region consistent with field RRLs at a similar metallicity that exhibit subsolar $[X/Fe]$ in Mg, Ca, Y, and Ba. Moreover, we found a striking underabundance in Sc: $[Sc/Fe] = -0.40 \pm 0.05$ for the RRL versus $[Sc/Fe] = +0.18 \pm 0.05$ for the OC stars. Scandium was not analyzed in the previous work by D’Orazi et al. (2024). However, Chadid et al. (2017) reported a strong declining trend of $[Sc/Fe]$ with $[Fe/H]$ in their sample of RRLs, with metal-rich RRLs showing a significant Sc underabundance (see Figure D.1). Our star follows this trend closely, matching their results.

The origin of these unusual abundances remains unclear, but we speculate that they may be linked to the formation scenario of young metal-rich RRLs. In particular, binary interactions and mass transfer involving a circumbinary disk could produce chemical peculiarities similar to those observed in post-AGB stars (Kamath & Van Winckel 2019; Mohorian et al. 2025). Making further progress on this topic will require quantitative modeling of circumbinary disks (including their structure, evolution, and dust–gas separation processes) coupled with binary-evolution calculations tailored to young metal-rich RRL progenitors. Even more important will be the analysis of statistically significant samples of RR Lyrae stars in order to robustly characterize the incidence and abundance patterns of

the observed anomalies. These aspects will be addressed in a forthcoming study.

Formation scenario – Our study offers definitive confirmation, verified through kinematics and elemental abundances, of the association between the RRL identified by M25 and the intermediate-age cluster Trumpler 5 ($\tau = 2.5$ Gyr). This association poses significant challenges in understanding the formation of these objects at such a young age, as single stellar evolution models are insufficient. To explain the properties of metal-rich RR Lyrae stars in the Galactic bulge and in relatively metal-rich globular clusters, He enrichment is often proposed (see, e.g., Savino et al. 2020). However, confirmation of He enrichment based on pulsation properties has not been obtained in any of these environments (Marconi & Minniti 2018; Li et al. 2025). In addition, He enrichment models generally predict higher luminosities and longer periods compared to field RRLs (see, e.g., Marconi et al. 2018; Bhardwaj et al. 2022). Indeed, all RRLs in metal-rich globular clusters exhibit longer periods than field RRLs of similar metallicity (Pritzl et al. 2000; Cruz Reyes et al. 2024). This is not consistent with Mateu’s star.

Bobrick et al. (2024) predicted the formation of metal-rich RR Lyrae stars as a consequence of binary interactions (see also Karczmarek et al. 2017). Key predictions from these models are that most metal-rich RR Lyrae stars, particularly the younger cohort (ages below 9 Gyr), currently reside in low-mass binary systems with orbital periods ranging from approximately 900 to 2000 days. While this is consistent with the Galactic kinematics and formation rates of most metal-rich RR Lyrae stars (see, e.g., Zhāng et al. 2025; Cabrera-Gadea et al. 2025), and while the same model also agrees with the detailed observations of binary hot subdwarfs (Vos et al. 2020; Molina et al. 2026), a definitive confirmation of RRL binary companions is still lacking, including in Gaia DR3 data (Iorio et al. 2026; see also Nagarajan et al. 2026). For the current mass of $M_{\text{rl}} = 0.55 M_{\odot}$, the potential companion mass of $1.5 M_{\odot}$, and a period of $P = 2000$ days suggested by the model assuming the cluster age, the semi-amplitude of the RV variation (K) of RRL is 15.71 km s^{-1} (for a circular orbit with an inclination of 90 degrees). Given our approximately 120-day observational time span, we expect a signal of around 2.9 km s^{-1} . This signal magnitude remains consistent with the additional scatter of roughly $\sim 2 \text{ km s}^{-1}$ required to fit the RV template, although it allows us to somewhat exclude the presence of more massive companions and/or shorter orbital periods. We plan to conduct a rigorous RV follow-up in the forthcoming months to better constrain possible binary properties.

Acknowledgements. Based on observations collected with PEPSI at the Large Binocular Telescope (DDT observations on October 2025–February 2026; GHOST at Gemini (November 2025–February 2026, programs GS-2025B-Q-415 and GS-2026A-Q-116); UVES at VLT (program 074.D-0344)). Our thanks to Chris Sneden and Márcio Catelan for insightful comments and suggestions. Based on observations obtained at the international Gemini Observatory, a program of NSF NOIRLab, which is managed by the Association of Universities for Research in Astronomy (AURA) under a cooperative agreement with the U.S. National Science Foundation on behalf of the Gemini Observatory partnership: the U.S. National Science Foundation (United States), National Research Council (Canada), Agencia Nacional de Investigación y Desarrollo (Chile), Ministerio de Ciencia, Tecnología e Innovación (Argentina), Ministério da Ciência, Tecnologia, Inovações e Comunicações (Brazil), and Korea Astronomy and Space Science Institute (Republic of Korea). This work made extensive use of CDS and NASA ADS databases. AB, VD acknowledge support from INAF Minigrant 2022, 2024. CM acknowledges funding from RDT and CSIC MIA programs from the Universidad de la República, Uruguay. GI was supported by a fellowship grant from the la Caixa Foundation (ID 100010434). AB acknowledges support from the Australian Research Council (ARC) Centre of Excellence for Gravitational Wave Discovery (OzGrav), through project number

CE230100016. The fellowship code is LCF/BQ/PI24/12040020. AN acknowledges the contribution of NextGenerationEU funds within the National Recovery and Resilience Plan (PNRR), Mission 4-Education and Research, Component 2-From Research to Business (M4C2), Investment Line 3.1-Strengthening and creation of Research Infrastructures, Project IR0000034-“STILES”, CUP C33C22000640006. ST acknowledges support from the INAF research project LBT-Supporto Arizona Italia.

References

- Amarsi, A. M., Lind, K., Osorio, Y., et al. 2020, *A&A*, 642, A62
 Bhardwaj, A., Kanbur, S. M., Rejkuba, M., et al. 2022, *A&A*, 668, A59
 Blanco-Cuaresma, S., Soubiran, C., Heiter, U., & Jofré, P. 2014, *Astrophysics Source Code Library* [record ascl:1409.006]
 Bobrick, A., Iorio, G., Belokurov, V., et al. 2024, *MNRAS*, 527, 12196
 Bono, G., Braga, V. F., Fabrizio, M., et al. 2026, *ApJ*, 998, 86
 Cabrera-Gadea, M., Mateu, C., & Ramos, P. 2025, *A&A*, 701, A136
 Caliskan, S., Amarsi, A. M., Racca, M., et al. 2025, *A&A*, 696, A210
 Cantat-Gaudin, T., Anders, F., Castro-Ginard, A., et al. 2020, *VizieR On-line Data Catalog: J/A+A/640/A1*
 Catelan, M., & Smith, H. A. 2015, *Pulsating Stars* (Weinheim: Wiley-VCH)
 Chadid, M., Sneden, C., & Preston, G. W. 2017, *ApJ*, 835, 187
 Cruz Reyes, M., Anderson, R. I., Johansson, L., Netzel, H., & Medaric, Z. 2024, *A&A*, 684, A173
 Cuevas-Otahola, B., Mateu, C., Cabrera-Ziri, I., et al. 2025, *MNRAS*, 541, 1434
 D’Odorico, S., Cristiani, S., Dekker, H., et al. 2000, *SPIE Conf. Ser.*, 4005, 121
 Donati, P., Coccozza, G., Bragaglia, A., et al. 2015, *MNRAS*, 446, 1411
 D’Orazi, V., Baratella, M., Lugaro, M., Magrini, L., & Pignatari, M. 2022, *Universe*, 8, 110
 D’Orazi, V., Storm, N., Casey, A. R., et al. 2024, *MNRAS*, 531, 137
 For, B.-Q., Preston, G. W., & Sneden, C. 2011, *ApJS*, 194, 38
 Garofalo, A., Delgado, H. E., Sarro, L. M., et al. 2022, *MNRAS*, 513, 788
 Green, G. M., Schlafly, E., Zucker, C., Speagle, J. S., & Finkbeiner, D. 2019, *ApJ*, 887, 93
 Gustafsson, B., Edvardsson, B., Eriksson, K., et al. 2008, *A&A*, 486, 951
 Iorio, G., & Belokurov, V. 2021, *MNRAS*, 502, 5686
 Iorio, G., Nagarajan, P., Bobrick, A., et al. 2026, *A&A*, submitted [arXiv:2603.20429]
 Kalari, V. M., Diaz, R. J., Robertson, G., et al. 2024, *AJ*, 168, 208
 Kamath, D., & Van Winckel, H. 2019, *MNRAS*, 486, 3524
 Karczmarek, P., Wiktorowicz, G., Ikkiewicz, K., et al. 2017, *MNRAS*, 466, 2842
 Lallement, R., Vergely, J. L., Babusiaux, C., & Cox, N. L. J. 2022, *A&A*, 661, A147
 Layden, A. C. 1995, *AJ*, 110, 2312
 Li, L.-J., Qian, S.-B., Zhu, L.-Y., Shi, X.-D., & Liao, W.-P. 2025, *MNRAS*, 542, 1791
 Mallinson, J. W. E., Lind, K., Amarsi, A. M., & Youakim, K. 2024, *A&A*, 687, A5
 Marconi, M., & Minniti, D. 2018, *ApJ*, 853, L20
 Marconi, M., Coppola, G., Bono, G., et al. 2015, *ApJ*, 808, 50
 Marconi, M., Bono, G., Pietrinferni, A., et al. 2018, *ApJ*, 864, L13
 Mashonkina, L. I., & Romanovskaya, A. M. 2022, *Astron. Lett.*, 48, 455
 Mateu, C., Cuevas-Otahola, B., & José Downes, J. 2025, *A&A*, in press, <https://doi.org/10.1051/0004-6361/202557438>
 Mohorian, M., Kamath, D., Menon, M., et al. 2025, *PASA*, 42, e151
 Molina, F., Vos, J., Bobrick, A., & Vučković, M. 2026, *A&A*, submitted [arXiv:2602.05008]
 Nagarajan, P., El-Badry, K., Bobrick, A., et al. 2026, *PASP*, submitted [arXiv:2602.21289]
 Narloch, W., Hajdu, G., Pietrzyński, G., et al. 2024, *A&A*, 689, A138
 Neeley, J. R., Marengo, M., Freedman, W. L., et al. 2019, *MNRAS*, 490, 4254
 Özdemir, S., Afşar, M., Sneden, C., et al. 2025, *A&A*, 699, A208
 Piskunov, N., & Valentí, J. A. 2017, *A&A*, 597, A16
 Preston, G. W. 1964, *ARA&A*, 2, 23
 Pritzl, B., Smith, H. A., Catelan, M., & Sweigart, A. V. 2000, *ApJ*, 530, L41
 Prudil, Z., Dékány, I., Grebel, E. K., & Kunder, A. 2020, *MNRAS*, 492, 3408
 Prudil, Z., Smolec, R., Kunder, A., Koch-Hansen, A. J., & Dékány, I. 2024, *A&A*, 685, A153
 Savino, A., Koch, A., Prudil, Z., Kunder, A., & Smolec, R. 2020, *A&A*, 641, A96
 Strassmeier, K. G., Ilyin, I., Järvinen, A., et al. 2015, *Astron. Nachr.*, 336, 324
 Virtanen, P., Gommers, R., Oliphant, T. E., et al. 2020, *Nat. Med.*, 17, 261
 Vos, J., Bobrick, A., & Vučković, M. 2020, *A&A*, 641, A163
 Wehrhahn, A., Piskunov, N., & Ryabchikova, T. 2023, *A&A*, 671, A171
 Zhāng, H., Iorio, G., Belokurov, V., et al. 2025, *MNRAS*, 544, 2493
 Zinn, R., Chen, X., Layden, A. C., & Casetti-Dinescu, D. I. 2020, *MNRAS*, 492, 2161

Appendix A: Log of observations and radial velocities

In Table A.1 we report information on the acquired spectra with PEPSI and GHOST, including the Julian Date, the phase of the spectra, the wavelength range, the average S/N ratios per pixel and the RV values.

Appendix B: Line list and spectral synthesis

For the derivation of atmospheric parameters and stellar abundances, the line list provided in Table B.1 was utilized. This table contains the wavelengths, species, excitation potentials (E.P.), and transition probabilities ($\log gf$) in columns 1, 2, 3, and 4, respectively. In Figure B.1 we show an example of the spectral fitting for the GHOST spectrum of our RRL. The figure compares the observed GHOST spectrum with the best-fit synthetic spectrum computed with PySME, obtained by simultaneously fitting the stellar atmospheric parameters and $[Fe/H]$. Several Fe I and Fe II lines within this narrow wavelength interval are marked.

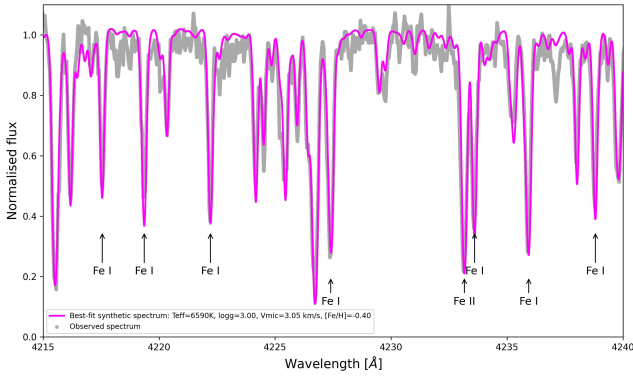


Fig. B.1. Comparison between observed (gray points) and synthetic (magenta continuous line) spectrum.

Appendix C: Comparison with cluster abundances

The atmospheric parameters and elemental abundances for our sample of RRL stars and the two RC stars in Trumpler 5 are detailed in Table C.1. Columns 1,2, and 3 are for the RRL Gaia DR3 3326852328563919744 and two RC stars in Trumpler 5, respectively. All elements are in NLTE except for Zn and Y since departure coefficients are not available in PySME. The errors represent internal uncertainties associated with the best-fit procedures. The errors on the mean values have been conservatively estimated as the average of the individual errors. Figure C.1 compares the $[X/H]$ abundance ratios of Mateu’s star with the OC mean derived from the two RC stars. While the overall abundance patterns are consistent, there are distinct discrepancies in Ca, Sc, Y, and Ba. We attribute these differences to the peculiar origin of this star.

Appendix D: Scandium abundances

In Figure D.1, we present the $[Sc/Fe]$ ratio of our star alongside the RRab sample from Chadid et al. (2017). We observe that our target RRL, notable for its significant subsolar Sc content, aligns well with the abundance trend defined by field metal-rich RRLs.

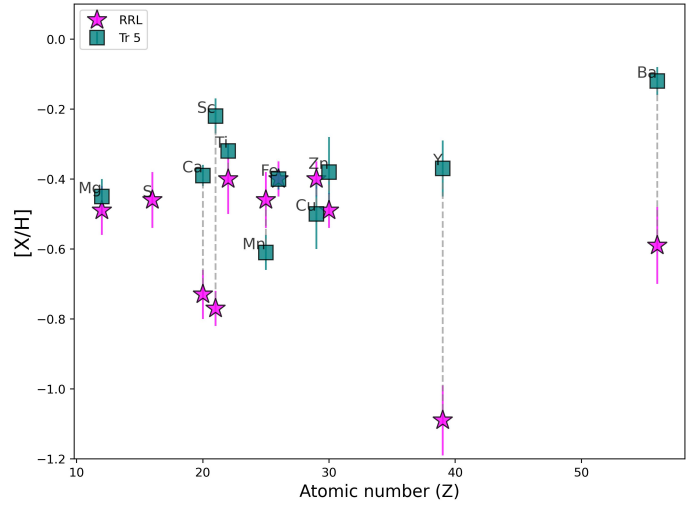


Fig. C.1. Comparison between the RRL and open cluster Trumpler 5 for the full suite of inferred elemental abundances.

The NLTE corrections, omitted in Chadid et al. (2017), are negligible for Sc II lines at the atmospheric parameters (temperature, gravity, metallicity) characteristic of metal-rich RRLs ($\lesssim 0.05$ dex).

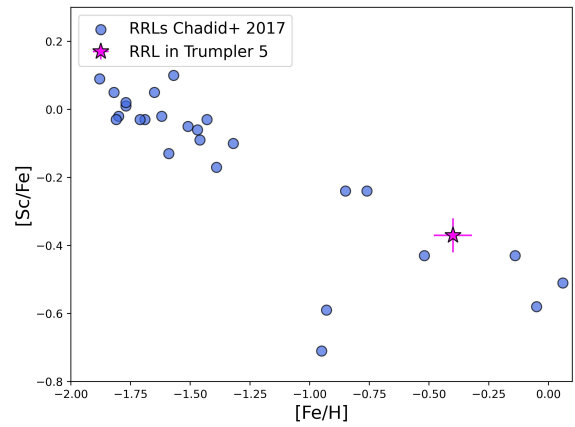


Fig. D.1. $[Sc/Fe]$ as a function of metallicity for the RRL sample by Chadid et al. (2017) and our RRL in Trumpler 5.

Appendix E: Systemic velocities

The RV data was phase-folded assuming the star’s period $P = 0.524807$ d and epoch at maximum light ($HJD_0=2457000.44368$ d) reported by the OGLE-IV database, and transformed to Barycentric Julian Date. The OGLE-IV data were chosen as the reference since it provides the best sampled light curve currently available for the star (see Fig. 1 in M25).

The RV template from Prudil et al. (2024) was fitted to the phase-folded RV data, assuming a simple model with Gaussian uncertainties. Following Prudil et al. (2024), we take the zero-point of the fit as the systemic velocity of the star, corresponding to the point of zero RV in the template occurring at $\phi = 0.35$. We also treat the amplitude of the RV curve, $AmpRV$, as a free parameter in our model, taking advantage of the good

Table A.1. Spectroscopic observations alongside pulsational phase (Φ) and individual RV measurements with associated uncertainties. The two spectra analyzed for abundances are highlighted.

Spectrum ID	Julian Date	Φ	Wavelength range [nm]	S/N [pix ⁻¹]	RV [km s ⁻¹]
PEPSI at LBT					
pepsib.20251025.000	2460973.935966	0.340	382-426	10	48.61 ± 0.14
pepsir.20251025.000	2460973.935966	0.340	624-742	110	48.85 ± 0.15
pepsib.20251025.001	2460973.957165	0.380	422-477	20	52.53 ± 0.18
pepsir.20251025.001	2460973.957165	0.380	536-627	103	52.60 ± 0.16
pepsib.20251214.056	2461023.782983	0.327	383-426	8	47.20 ± 0.80
pepsir.20251214.036	2461023.782983	0.327	624-742	106	49.16 ± 0.78
pepsib.20251214.057	2461023.804165	0.368	422-477	20	51.79 ± 0.25
pepsir.20251214.037	2461023.804165	0.368	536-627	113	51.31 ± 0.25
pepsir.20251214.040	2461023.894412	0.540	536-627	15	60.14 ± 0.28
pepsir.20260205.002	2461076.780448	0.310	536-627	50	47.31 ± 0.48
pepsir.20260205.003	2461076.811965	0.370	536-627	50	51.99 ± 0.48
GHOST at Gemini-S					
S20251109S0153_blue	2460988.846577	0.754	347-544	20	74.58 ± 0.34
S20251109S0153_red	2460988.846577	0.754	521-1061	40	74.97 ± 0.45
S20251111S0090_blue	2460990.835672	0.544	347-544	14	62.46 ± 0.26
S20251111S0090_red	2460990.835672	0.544	521-1061	45	62.84 ± 0.37
S20260211S0052_blue	2461082.539757	0.284	347-544	80	44.54 ± 0.20
S20260211S0052_red	2461082.539757	0.284	521-1061	110	44.87 ± 0.20

phase coverage provided by our observations. We include an extra velocity dispersion σ_x term (added to the RV uncertainties in quadrature) to account for a possible underestimation of the RV errors and/or additional (possibly physical) sources of uncertainty. Uniform priors were assumed for all parameters, in the ranges $V_y \in [-500, 500]$ km s⁻¹, $\text{AmpRV} \in [0, 150]$ km s⁻¹ and $\sigma_x \in [0, 50]$ km s⁻¹.

Figure E.1 shows the phase-folded RV curve with the best-fitting model (left plot, top panel) and residuals (left plot, bottom panel) and the corner plot with 1-D and 2-D posterior probability density functions (PDF) for the fit parameters (right plot). The best-fitting value is taken as the maximum-a-posteriori (MAP) of the 3D (joint) PDF, and the uncertainties reported correspond to the 14th and 86th percentiles of the marginal distributions, respectively.

Appendix F: Color-magnitude diagram

Figure F.1 shows the color-magnitude diagram in the Gaia bands for the cluster population. The insert shows the H-R diagram in a zoomed-in view around the RRL star at $\phi \approx 0.3$, the phase at which the star’s temperature was inferred. This shows the RRL is well inside the instability strip and supports the adoption of the extinction ($A_V = 1.65$) from the Green et al. (2019) 3D dustmap from M25, rather than the lower extinction ($A_V = 1.5$) predicted from the Lallement et al. (2022) dust map which placed the star just past the edge of the instability strip.

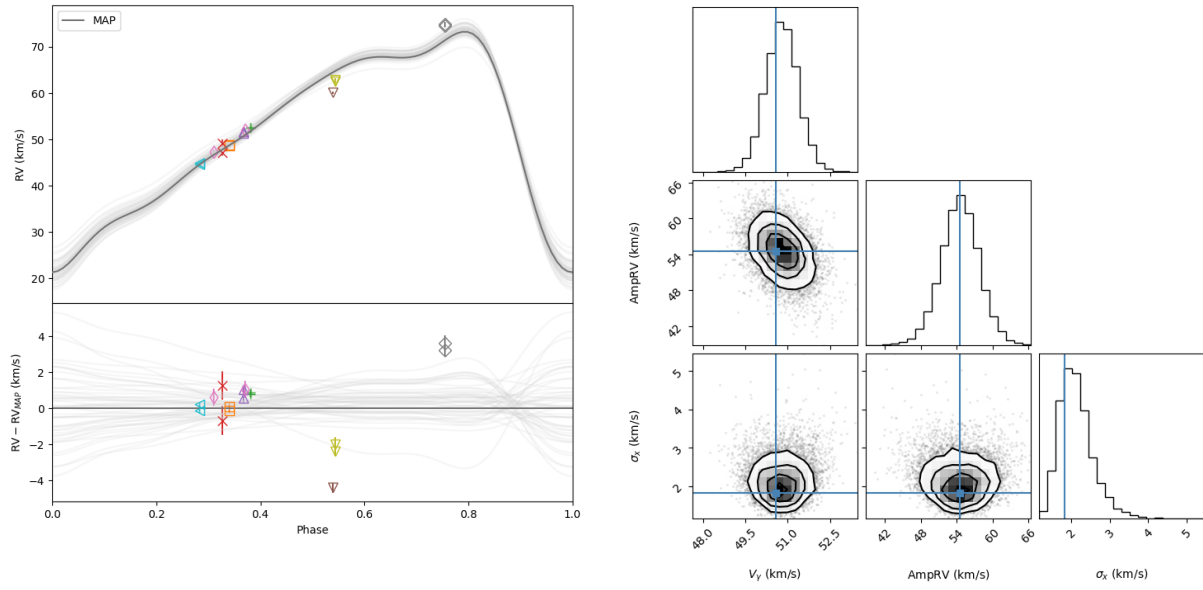


Fig. E.1. Radial velocity (top) and best-fit residuals (bottom) as a function of phase. The best-fitting template (MAP) is shown by the dark solid line. Light gray lines correspond to 50 random draws from the posterior PDF. Different symbols correspond to different observation epochs, with the two observations corresponding to the spectra from the blue/red channels at the same epoch sharing the same symbol. Error bars for the RVs are shown, but are typically smaller than the symbols. *Right panel:* Corner plot showing the marginal 2-D and 1-D posterior PDFs for the three free parameters: systemic velocity V_γ , amplitude of the RV curve AmpRV and the additional velocity dispersion term σ_x . The solid (blue) line corresponds to the MAP of the (joint) 3D posterior PDF.

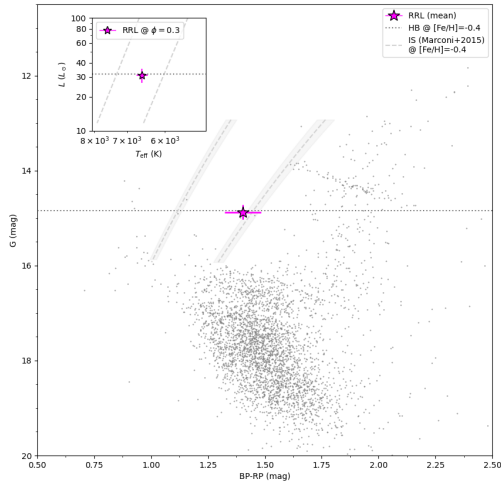


Fig. F.1. Color-magnitude diagram for the Trumpler 5 OC. The mean position (intensity-averaged magnitude and color) of the RRL is shown with the (magenta) star. Cluster members from Cantat-Gaudin et al. (2020) are shown as (gray) dots. The dashed and dotted lines correspond to the instability strip limits from Marconi et al. (2015) and horizontal branch magnitude from the Garofalo et al. (2022) period-luminosity-metallicity relation at the star’s metallicity, distance and extinction of $A_V = 1.65 \pm 0.15$ following M25 (see their Sec.3 for details). The insert shows the H-R diagram and the position of the star at $\phi = 0.3$

Table B.1. Line list used for atmospheric parameter and elemental abundance determinations. **Table B.1.** continued.

Wavelength [Å]	Ion	E.P. [eV]	log <i>gf</i>	Wavelength [Å]	Ion	E.P. [eV]	log <i>gf</i>
4217.545	Fe 1	3.43	-0.48	4233.162	Fe 2	2.58	-1.90
4219.359	Fe 1	3.57	0.00	4273.320	Fe 2	2.70	-3.30
4222.213	Fe 1	2.45	-0.97	4296.566	Fe 2	2.70	-2.93
4240.784	Fe 1	4.37	-2.35	4385.377	Fe 2	2.78	-2.68
4271.760	Fe 1	1.48	-0.16	4416.819	Fe 2	2.78	-2.41
4282.403	Fe 1	2.18	-0.78	4491.397	Fe 2	2.86	-2.70
4352.734	Fe 1	2.22	-1.29	4508.280	Fe 2	2.86	-2.25
4375.929	Fe 1	0.00	-3.03	4515.333	Fe 2	2.84	-2.45
4383.544	Fe 1	1.48	0.20	4520.218	Fe 2	2.81	-2.60
4388.407	Fe 1	3.60	-0.68	4541.516	Fe 2	2.86	-2.79
4404.750	Fe 1	1.56	-0.14	4576.333	Fe 2	2.84	-2.92
4427.309	Fe 1	0.05	-2.92	4582.830	Fe 2	2.84	-3.09
4432.567	Fe 1	3.57	-1.60	4583.829	Fe 2	2.81	-1.86
4447.717	Fe 1	2.22	-1.34	4620.513	Fe 2	2.83	-3.24
4514.184	Fe 1	3.05	-2.05	4629.331	Fe 2	2.81	-2.33
4574.215	Fe 1	3.21	-2.50	4993.350	Fe 2	2.81	-3.64
4602.001	Fe 1	1.61	-3.15	5264.802	Fe 2	3.23	-3.12
4602.940	Fe 1	1.48	-2.21	6084.102	Fe 2	3.20	-3.78
4607.645	Fe 1	3.98	-3.24	6149.246	Fe 2	3.89	-2.72
4619.288	Fe 1	3.60	-1.12	6432.676	Fe 2	2.89	-3.52
4630.120	Fe 1	2.28	-2.59	4913.613	Ti 1	1.87	0.22
4647.434	Fe 1	2.95	-1.35	4981.731	Ti 1	0.85	0.57
4661.970	Fe 1	2.99	-2.50	5219.702	Ti 1	0.02	-2.22
5217.389	Fe 1	3.21	-1.07	5689.460	Ti 1	2.30	-0.36
5364.870	Fe 1	4.45	0.23	5978.541	Ti 1	1.87	-0.31
5569.618	Fe 1	3.42	-0.49	6091.171	Ti 1	2.27	-0.45
5576.089	Fe 1	3.43	-1.00	4874.009	Ti 2	3.09	-0.86
5638.262	Fe 1	4.22	-0.87	5211.530	Ti 2	2.59	-1.41
5679.023	Fe 1	4.65	-0.90	5381.022	Ti 2	1.57	-1.97
5705.464	Fe 1	4.30	-1.36	5418.768	Ti 2	1.58	-2.13
5778.453	Fe 1	2.59	-3.43	5528.405	Mg 1	4.35	-0.50
5855.075	Fe 1	4.61	-1.48	5711.088	Mg 1	4.35	-1.72
5883.816	Fe 1	3.96	-1.36	6743.580	S 1	7.87	-1.03
5916.247	Fe 1	2.45	-2.99	6748.790	S 1	7.87	-0.53
5956.693	Fe 1	0.86	-4.61	6757.150	S 1	7.87	-0.24
6056.004	Fe 1	4.73	-0.46	5588.749	Ca 1	2.53	0.36
6151.617	Fe 1	2.18	-3.30	6122.217	Ca 1	1.89	-0.32
6165.359	Fe 1	4.14	-1.47	6161.297	Ca 1	2.52	-1.27
6240.646	Fe 1	2.22	-3.23	5526.770	Sc 2	1.77	0.02
6246.318	Fe 1	3.60	-0.73	5640.989	Sc 2	1.50	-1.13
6315.811	Fe 1	4.08	-1.71	5657.906	Sc 2	1.51	-0.54
6336.823	Fe 1	3.69	-0.86	6013.475	Mn 1	3.07	-0.25
6380.743	Fe 1	4.19	-1.38	6016.643	Mn 1	3.07	-0.20
6494.980	Fe 1	2.40	-1.27	6021.747	Mn 1	3.08	0.06
				5105.542	Cu 1	1.39	-1.54
				4722.153	Zn 1	4.03	-0.34
				4883.682	Y 2	1.08	-0.30
				5853.669	Ba 2	0.60	-3.01
				6141.709	Ba 2	0.70	-2.26

Table C.1. Stellar parameters and abundance ratios ([X/H]).

	RRL	Cl* Tr5	Cl* Tr 5
	GHOST@Gemini	K 3-2553	K 3-3236
T_{eff} [K]	6590±150	4793±90	4863±60
$\log g$	3.00±0.10	2.39±0.08	2.71±0.10
V_{mic} [km s ⁻¹]	3.50±0.20	1.33±0.20	1.40±0.20
V_{mac} [km s ⁻¹]	9.50±0.50	4.53±0.26	4.89±0.38
[Mg/H]	-0.49 ± 0.02	-0.45 ± 0.10	-0.42 ± 0.10
[S/H]	-0.46 ± 0.08		
[Ca/H]	-0.73 ± 0.02	-0.40 ± 0.04	-0.37 ± 0.06
[Sc/H]	-0.80 ± 0.08	-0.25 ± 0.05	-0.18 ± 0.04
[Ti/H]	-0.40 ± 0.03	-0.35 ± 0.08	-0.29 ± 0.06
[Mn/H]	-0.46 ± 0.05	-0.61 ± 0.10	-0.60 ± 0.08
[Fe/H]	-0.40 ± 0.05	-0.42 ± 0.10	-0.37 ± 0.06
[Cu/H]	-0.40 ± 0.05	-0.48 ± 0.08	-0.51 ± 0.09
[Zn/H]	-0.49 ± 0.05	-0.46 ± 0.10	-0.30 ± 0.10
[Y/H]	-1.09 ± 0.10	-0.47 ± 0.11	-0.26 ± 0.09
[Ba/H]	-0.59 ± 0.10	-0.15 ± 0.08	-0.09 ± 0.06